Analyst

ROYAL SOCIETY OF CHEMISTRY

PAPER

View Article Online
View Journal | View Issue

Cite this: *Analyst*, 2024, **149**, 553

Spectral fingerprinting of cellular lipid droplets using stimulated Raman scattering microscopy and chemometric analysis†

Aurélie Rensonnet, [a,b] William J. Tipping, [a] Cedric Malherbe, [b] Karen Faulds, [a] Gauthier Eppe [b] and Duncan Graham *[a]

Hyperspectral stimulated Raman scattering (SRS) microscopy is a powerful method for direct visualisation and compositional analysis of cellular lipid droplets. Here we report the application of spectral phasor analysis as a convenient method for the segmentation of lipid droplets using the hyperspectral SRS spectrum in the high wavenumber and fingerprint region of the spectrum. Spectral phasor analysis was shown to discriminate six fatty acids based on vibrational spectroscopic features in solution. The methodology was then applied to studying fatty acid metabolism and storage in a mammalian cancer cell model and during drug-induced steatosis in a hepatocellular carcinoma cell model. The accumulation of fatty acids into cellular lipid droplets was shown to vary as a function of the degree of unsaturation, whilst in a model of drug-induced steatosis, the detection of increased saturated fatty acid esters was observed. Taking advantage of the fingerprint and high wavenumber regions of the SRS spectrum has yielded a greater insight into lipid droplet composition in a cellular context. This approach will find application in the label-free profiling of intracellular lipids in complex disease models.

Received 3rd October 2023,
Accepted 6th December 2023

DOI: 10.1039/d3an01684f

rsc.li/analyst

Introduction

Lipid droplets (LDs) are intracellular reservoirs for excess lipids, predominantly fatty acids (FAs) and cholesterol esters (CEs) that are encircled by a phospholipid monolayer decorated with a number of proteins.[1] FAs are an important molecular class because they represent the main building blocks of several lipid species, including phospholipids, sphingolipids and triglycerides.[2,3] FAs are composed of a carboxylic acid group and a hydrocarbon acyl chain of varying carbon lengths (typically, C_{11}–C_{20} are the most abundant in mammalian cellular LDs)[4] and varying degrees of saturation, which impacts their biological properties and functions.[5,6] The importance of altered fatty acid metabolism in cancer has received renewed interest because FAs have been shown to play an integral role in tumorigenesis.[7] For example, the increased reliance of cancer cells on *de novo* FA biosynthesis and exogenous FA uptake has been shown to sustain a rapid proliferative rate and to provide an essential energy source during conditions of metabolic stress.[8]

Conventional methods for the analysis of lipid composition include mass spectrometry[9] and nuclear magnetic resonance spectroscopy,[10] however, these techniques lack subcellular spatial information. Whereas fluorescence imaging can permit super-resolution spatial visualisation, the use of hydrophobic dyes as contrast agents fundamentally lacks compositional information. Taken together, these techniques are unable to achieve the required spatial resolution or molecular specificity to elucidate how LDs are formed and metabolised, or to decipher intracellular function of LDs in disease onset and progression.

Advances in stimulated Raman scattering (SRS) microscopy have driven performance limits for Raman imaging in all aspects including speed, sensitivity, and spatial and lateral resolution for biological characterisation.[11–13] Raman imaging is a powerful method for studying intracellular lipids, membrane phase behaviour and lipid organisation.[14] For example, a recent report demonstrated quantitative chemical imaging of FAs based on chain length using C–C *gauche* modes in the region 1050–1140 cm^{-1} of the SRS spectrum.[15] With a spectral resolution <10 cm^{-1}, hyperspectral analysis was capable of discriminating mixtures of FAs in neat form using multivariate curve resolution, although the use of a femtosecond laser source for imaging is known to be cell damaging, which can

[a]*Centre for Molecular Nanometrology, WestCHEM, Department of Pure and Applied Chemistry, Technology and Innovation Centre, University of Strathclyde, Glasgow, G1 1RD, UK. E-mail: duncan.graham@strath.ac.uk*
[b]*Mass Spectrometry Laboratory, MolSys Research Unit, University of Liège, Allée du 6 Août, 4000 Liège, Belgium*

† Electronic supplementary information (ESI) available: Fig. S1. See DOI: https://doi.org/10.1039/d3an01684f

limit some live cell applications.[16] Despite numerous studies demonstrating the power of SRS imaging for visualising LDs in mammalian cells,[17–19] tissues[20] and organisms,[21] the technique has rarely been used to study FA storage without the use of bioorthogonal tagging based on deuterium[22–25] or alkyne modifications.[26–28] The use of chemometric analysis techniques including *k*-means cluster analysis[29–31] and spectral phasor analysis[32–38] have been applied to extricate the underlying biological features contained within hyperspectral SRS imaging datasets in a label-free way. As such, we proposed that chemometric analysis of hyperspectral SRS datasets could enable imaging of FA uptake and storage without exogenous tagging.

Here, we demonstrate that hyperspectral SRS imaging coupled to spectral phasor analysis is a powerful method for the label-free discrimination of fatty acids in pure form, and for compositional analysis of intracellular lipid droplets in a cancer cell model as well as under conditions of cellular steatosis in a hepatocellular carcinoma cell model. We demonstrate the first use of spectral phasor analysis using the high wavenumber and fingerprint regions of the Raman spectrum for a greater insight into lipid droplet characterisation.

Experimental

Reagents and chemicals

Stearic acid (>99%), elaidic acid (≥99.0%), oleic acid (≥99%), linoleic acid (≥99%), linolenic acid (≥99%) and stearidonic acid (≥99%) were purchased from Sigma Aldrich and were used as supplied. A stock solution of each acid was prepared in anhydrous DMSO (Fisher Scientific) at a concentration of 20 mM. Cyclosporin A (97.0–101.5% (on dried basis), Sigma Aldrich) was dissolved in anhydrous DMSO at a concentration of 10 mM.

Cell culture

HepG2 cells (HB-8065™) were received from the European Collection of Authenticated Cell Cultures (ECACC). HeLa cells were gifted from the Strathclyde Institute of Pharmacy and Biomedical Sciences (Glasgow) as a subculture from a stock acquired from the ECACC. Both cell lines were cultured in Dulbecco's Modified Eagle Medium (DMEM; GIBCO™, Fisher Scientific) supplemented with 10% foetal bovine serum (FBS, Gibco™, Fisher Scientific), 1% penicillin/streptomycin (Gibco™, 10 000 U mL^{-1}, Fisher Scientific) and 1% amphotericin B (Gibco™, 250 μg mL^{-1}, Fisher Scientific). Cells were maintained at 37 °C and 5% CO_2 in a humidified incubator and were routinely sub-cultured at *ca.* 80% confluency.

HeLa or HepG2 cells were plated at 2.5×10^5 cells per well in 6-well plates (Fisher Scientific) containing a glass coverslip (22 × 22 mm, #1.5H, Thorlabs) in DMEM (2 mL). The cells were incubated for 24 hours at 37 °C with 5% CO_2 prior to treatment. After 24 hours, the medium was removed, and the cells were treated as follows:

Fatty acid treatment. In each case, the 20 mM fatty acid stock solutions in DMSO were diluted in a 5 wt% solution of bovine serum albumin (BSA, Fisher Scientific) in PBS (Oxoid™, Fisher Scientific) (1 : 4 v/v) to improve the solubility of the FAs. DMEM was then added to the solution to obtain of final volume of DMEM/FA/BSA of 2 mL and a final concentration of FAs in the range 100–400 μM. The cells were treated with FA-containing media (2 mL) at 37 °C with 5% CO_2 for 24 hours.

Cyclosporin A (CyA) treatment. HepG2 cells were treated with 30 μM of CyA from the 10 mM of the stock solution in DMSO diluted in DMEM (6 μL of solution in 2 mL of DMEM). The control cells were treated with DMSO only (6 μL in 2 mL of DMEM). After 24 or 48 hours, the enriched medium was removed, and the cells were washed with PBS (2 mL). The cells were then fixed with 4% paraformaldehyde in PBS (PFA, from 16% PFA stock, Pierce™, Fisher Scientific, 2 mL) for 10 minutes at 37 °C and 5% CO_2, prior to washing with PBS (2 mL). The coverslips were mounted on microscope glass slides with a PBS boundary between the glass layers.

SRS microscopy

An integrated laser system (picoEmerald™ S, Applied Physics & Electronics, Inc.) was used to produce two synchronised laser beams at 80 MHz repetition rate. A fundamental Stokes beam (1031.4 nm, 2 ps pulse width) was intensity modulated by an electro-optic-modulator (EoM) with >90% modulation depth, and a tunable pump beam (700–960 nm, 2 ps pulse width, <1 nm (~10 cm^{-1}) spectral bandwidth) was produced by a built-in optical parametric oscillator. The pump and Stokes beams were spatially and temporally overlapped using two dichroic mirrors and a delay stage inside the laser system and coupled into an inverted laser-scanning microscope (Leica TCS SP8, Leica Microsystems) with optimised near-IR throughput. SRS images were acquired using a 40× objective (HC PL IRAPO 40×, N.A. 1.10 water immersion lens) with a 9.75–48 μs pixel dwell time over a 512 × 512 or a 1024 × 1024 frame. The Stokes beam was modulated with a 20 MHz EoM. Forward scattered light was collected by a S1 N.A. 1.4 condenser lens (Leica Microsystems). Images were acquired at 12-bit image depth. The laser powers measured after the objective lens were in the range 10–30 mW for the pump beam only, 10–50 mW for the Stokes beam only and 20–70 mW (pump and Stokes beams). The spatial resolution of the system is ~450 nm (pump wavelength = 792 nm). SRS spectra were acquired across the range 2800–3050 cm^{-1} (0.4 nm re-tune, 40 images) or 1200–1780 cm^{-1} (0.6 nm re-tune, 78 images). The spectra were corrected for wavenumber position (*x*-axis calibration) based on a lambda scan of polystyrene–PMMA beads in the region 3060 cm^{-1} (ν(=CH)).

Raman spectroscopy

The Raman reference spectra of the FAs were recorded using an inVia™ confocal Raman microscope (Renishaw) interfaced with a 532 nm DPSS laser. The spectra were acquired using a 20× objective (Leica Microsystems). For stearic, oleic and elaidic acids, the Raman spectra were measured with a 10 s exposure time, at 5% laser power (~1.8 mW) and using an

extended scan from 100 to 3200 cm^{-1}. The spectra of linoleic and linolenic acids were recorded with a 2 s exposure time (~36 mW), and for stearidonic acid, the Raman spectra were acquired using a 2 s exposure time (~3.6 mW). The confocal Raman microscope was interfaced with an 1800 lines per mm grating and a CCD detector. Prior to spectral acquisition, the instrument was calibrated using an internal standard of Si at 520.5 cm^{-1}.

Data processing

SRS images. False colour assignments, scale bars and image overlays were added to images using ImageJ software. Consistent brightness and contrast settings were used when comparing image datasets. For CH_2/CH_3 ratio imaging, a threshold (mask) image was first generated by adjusting threshold of the average intensity projection across the image stack on ImageJ, then non-zero values were normalized to one. CH_2 images were then divided by the corresponding CH_3 image, and the resulting ratio image multiplied with the mask image to create the final CH_2/CH_3 ratio image. The display range of CH_2/CH_3 ratio images is set to be 0–1.25 and are presented in the Rainbow RGB LUT.

Spectral phasor analysis. The SRS image data set across the range 2800–3050 cm^{-1} was imported into ImageJ and an average intensity projection was created. The spectral phasor analysis was performed as described by Fu *et al.* (ref. 32) using a plug-in for ImageJ as described previously (ref. 34). Segmentation of the phasor plot was performed manually using regions-of-interest to create images of discrete cellular locations. The corresponding mean spectra for the selected ROIs are plotted using Origin.

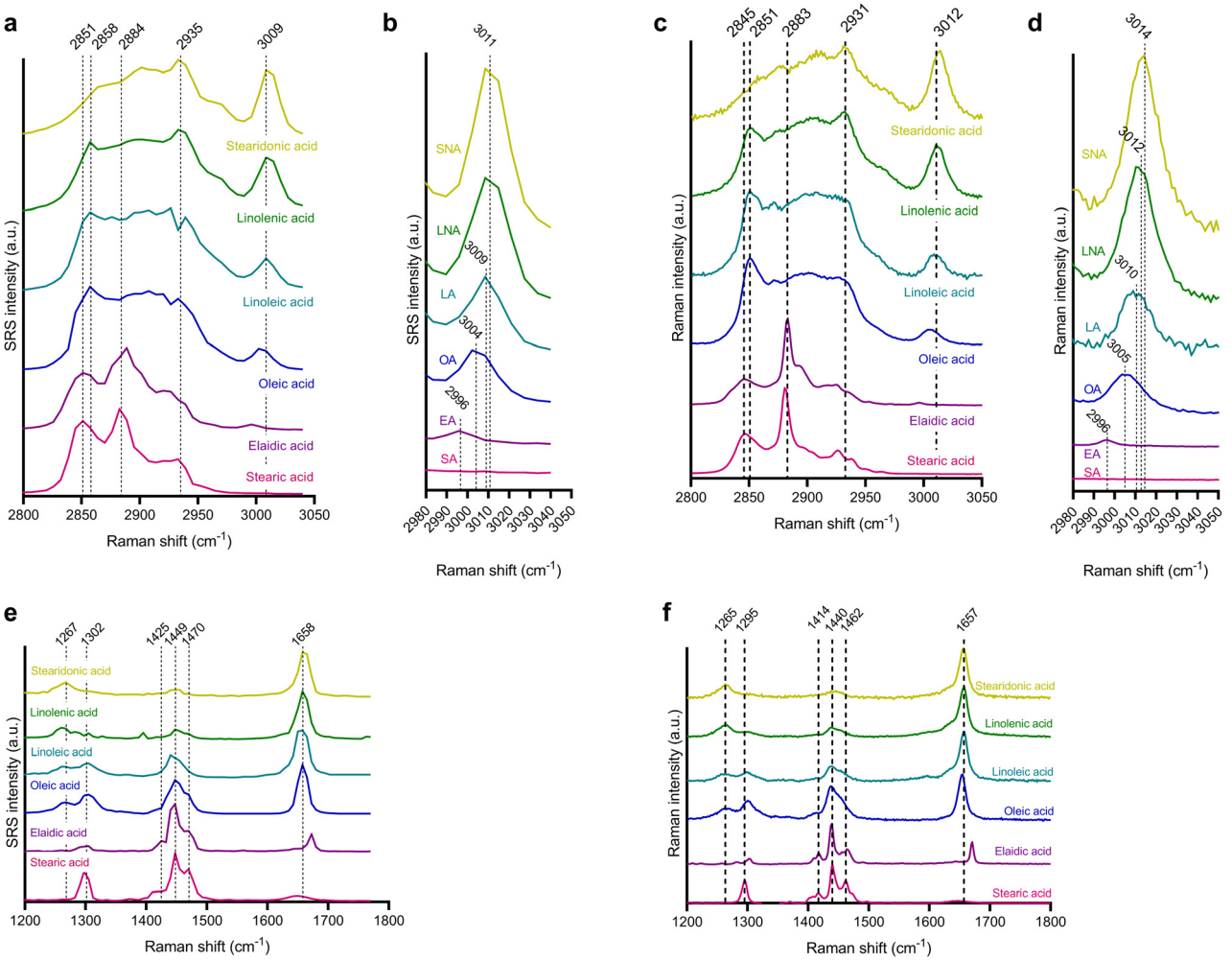

Fig. 1 Mean SRS and Raman spectra of six fatty acids in neat form. (a) SRS Spectra of the six fatty acids in neat form were acquired from 2800 to 3050 cm^{-1} by tuning the pump beam with a 0.4 nm step (~6.3 cm^{-1}). (b) Expansion of the SRS spectrum of the =CH stretching mode at ~3010 cm^{-1}. (c) Raman spectra of the six fatty acids were acquired using a 532 nm laser with a 20× lens. (d) Expansion of the Raman spectrum of the =CH stretching mode at ~3010 cm^{-1}. (e) Mean SRS spectra of the six studied fatty acids from 1200 to 1780 cm^{-1} by tuning the pump beam with a 0.6 nm step (~7.5 cm^{-1}). (f) Mean Raman spectra of the six studied fatty acids from 1200 to 1780 cm^{-1} were acquired using a 532 nm laser with a 20× lens for 10 s (1.8 mW stearic acid, elaidic acid, oleic acid), 2 s (36 mW linoleic acid and linolenic acid) and 2 s (3.6 mW stearidonic acid). All annotations are in cm^{-1}.

Results and discussion

The aim of this research was to investigate the use of hyperspectral SRS imaging for the identification and determination of the degree of unsaturation of FAs in cellular lipid droplets as biological hallmarks of cancer[39] and drug-induced steatosis (DIS).[40] Both cancer and DIS result in the deleterious elevation of FAs into intracellular lipid droplets, and we proposed that SRS microscopy could provide a label-free, *in situ* insight into each of these diseases. We first investigated the hyperspectral imaging of six fatty acids of the C18 family because of the relative abundance of C18 FAs in mammalian cells; for example, stearic acid (C18:0) is amongst the most abundant saturated FA in cells, whilst oleic acid (C18:1) is the most abundant monounsaturated intracellular FA.[6] Firstly, we compared the SRS spectra of stearic acid (C18:0), oleic acid (C18:1, *cis* unsaturation), elaidic acid (C18:1, *trans* unsaturation), linoleic acid (C18:2), linolenic acid (C18:3), and stearidonic acid (C18:4) to their respective spontaneous Raman spectra to ensure parity between the two techniques.

The SRS and Raman spectra from the neat samples are provided in Fig. 1 and Table 1. The high wavenumber region of the SRS spectrum corresponds to the C–H stretching normal modes which are assigned‡ at 2847–2883 cm^{-1} ($\nu(CH_2)$), 2900–2970 cm^{-1} ($\nu(CH_3)$), and 2996–3014 cm^{-1} (ν(=C–H)) (Fig. 1).[41] Due to the numerous chemically inequivalent C–H bonds in C18 FAs, the spectra in the high wavenumber region are broad, reflecting the overlapping nature of the Raman modes in this region. As the unsaturation degree increases from stearic acid (C18:0) to stearidonic acid (C18:4), a clear increase in the (ν(=C–H)) Raman band was detected, which showed a blue shifting with increasing unsaturation (Fig. 1b). Across the unsaturated FAs, the intensity of the 2851 cm^{-1} symmetric $\nu(CH_2)$ vibration relative to the other peaks in this region appears to decrease with increasing conjugated unsaturation (Fig. 1a). This result demonstrated that the intensity ratio of CH_2/CH_3 stretches decreases with an increasing degree of unsaturation. The symmetric $\nu(CH_3)$ band ~2935 cm^{-1} is clearly visible for linolenic acid (C18:3) and stearidonic acid (C18:4). When comparing the SRS spectra of elaidic acid (C18:1, *trans* unsaturation) with oleic acid (C18:1, *cis* unsaturation), several differences are apparent. Firstly, the relative intensity of the (ν(=C–H)) Raman mode is reduced in elaidic acid compared to oleic acid, whilst the ratio of the bands at ~2850 cm^{-1} to ~2880 cm^{-1} is reduced for elaidic acid when compared to oleic acid (Fig. 1b). Generally, the SRS spectrum of elaidic acid more closely resembles that of the saturated stearic acid. Altogether, the SRS spectra of the six FAs closely resemble the peak profile of the Raman spectra (Fig. 1c and d) albeit with a slight offset in the *x*-axis calibration in the SRS spectra (which is likely due to the reduced spectral resolution

‡ The following assignments have been applied in this manuscript: ν = stretching vibration; δ = deformation; β = bending; α = scissoring; τ = twisting.

Table 1 SRS and Raman assignments for the fatty acids used in this study. SRS bands are (bold)

	ν(=CH)	$\nu_s(CH_3)$	$\nu_{as}(CH_2)$	$\nu_s(CH_2)$	ν(C=C)	$\beta(CH_2/CH_3)$	$\alpha(CH_2/CH_3)$	$\beta(CH_2)$	$\tau(CH_2)$	δ(=C–H)
Stearic acid		2927 (**2935**)	2881 (**2884**)	2847 (**2851**)		1462 (**1470**)	1440 (**1449**)	1414 (**1425**)	1295 (**1302**)	
Oleic acid	3005 (**3004**)	2925 (**2935**)		2851 (**2858**)	1654 (**1658**)		1438 (**1449**)		1301 (**1302**)	1263 (**1267**)
Elaidic acid	2996 (**2996**)	2924 (**2935**)	2883 (**2884**)	2847 (**2851**)	1671 (**1672**)	1465 (**1470**)	1439 (**1449**)	1415 (**1425**)	1301 (**1302**)	
Linoleic acid	3010 (**3009**)	2930 (**2935**)		2851 (**2858**)	1657 (**1658**)		1440 (**1449**)		1300 (**1302**)	1264 (**1267**)
Linolenic acid	3012 (**3011**)	2932 (**2935**)		2852 (**2858**)	1657 (**1658**)				1300 (**1302**)	1265 (**1267**)
Stearidonic acid	3014 (**3011**)	2931 (**2935**)			1656 (**1658**)					1265 (**1267**)

of SRS imaging compared to spontaneous Raman spectroscopy).[42]

In the fingerprint region of the SRS spectrum (Fig. 1e), the unsaturated FAs displayed a prominent peak at ~1658 cm^{-1} corresponding to the ν(C=C) vibration, which is notably absent in stearic acid (C18:0) and is blue shifted in elaidic acid to 1672 cm^{-1}, reflecting the *trans* unsaturated nature of this FA. Between 1400–1500 cm^{-1}, several Raman bands in the SRS spectrum of stearic acid corresponding to the $\beta(CH_2/CH_3)$, $\alpha(CH_2/CH_3)$ and $\beta(CH_2)$ modes were detected at 1470 cm^{-1}, 1449 cm^{-1} and 1425 cm^{-1} respectively (Fig. 1e).[41] With increasing unsaturation, the resolution and intensity of these modes decreases, with the exception of elaidic acid which has an SRS spectrum that more closely resembles that of stearic acid than the *cis* unsaturated FAs. Finally, the spectra displayed two bands at 1302 cm^{-1} ($\tau(CH_2)$, stearic acid) and 1267 cm^{-1} (δ(=C–H), unsaturated FAs), from which the intensity ratio could be used to determine the unsaturation degree of a lipid sample (Fig. 1e).[41] Across the fingerprint region, the SRS spectra (Fig. 1e) closely resemble the Raman spectra (Fig. 1f).

Across the series of C18 FAs investigated in this work, several Raman bands were shown to vary in Raman shift and intensity. For example, the degree of unsaturation for FAs could be calculated using the following ratiometric intensity analysis: ν(=C–H)/$\nu(CH_2)$, ν(C=C)/$\alpha(CH_2/CH_3)$ and δ(=C–H)/$\tau(CH_2)$. Fig. 2 presents the ratiometric analysis of these key bands in the SRS and Raman spectra acquired in Fig. 1. The ratio ν(=C–H)/$\nu(CH_2)$ at ~3010/~2850 cm^{-1} shows a positive trend across the C18 FAs analysed reflecting the increasing degree of unsaturation from stearic acid to stearidonic acid. Similarly, a positive trend was observed for the Raman bands ν(C=C)/$\alpha(CH_2/CH_3)$ at ~1660/1440 cm^{-1} and δ(=C–H)/$\tau(CH_2)$ at 1267/1302 cm^{-1}, respectively. Across these three ratios, the SRS and Raman results are broadly similar, apart for the result of stearidonic acid (C18:4) (Fig. 2b and c) where a reduced ratio was detected in the SRS spectra compared to the Raman spectra. We attributed this discrepancy to sample degradation during the SRS spectral acquisition. The delay in retuning the optical parametric oscillator (OPO) in between image frames to construct the SRS spectrum (~10 min) compared to the Raman spectral acquisition (1 min) accounted for the degradation of stearidonic acid, which is light sensitive and typically stored at −20 °C. In conclusion, the SRS spectra showed a high degree of spectral similarity to the spontaneous Raman spectra, albeit with a slight offset in the *x*-axis due to the lower spectral resolution of the SRS imaging system.

Having demonstrated the suitability of hyperspectral SRS imaging for the analysis of FAs in neat form, we investigated the potential of spectral phasor analysis for the automated compositional analysis of cellular lipid droplets based on the SRS spectrum. Spectral phasor analysis is a Fourier transform-based technique that projects every pixel within a 3D hyperspectral SRS image stack (x, y, λ) as a point (or phasor) on the 2D phasor plane to provide an overview of the ensemble of pixels.[32] We created a hyperstack of the SRS spectra from the six FAs investigated in this study from which we performed

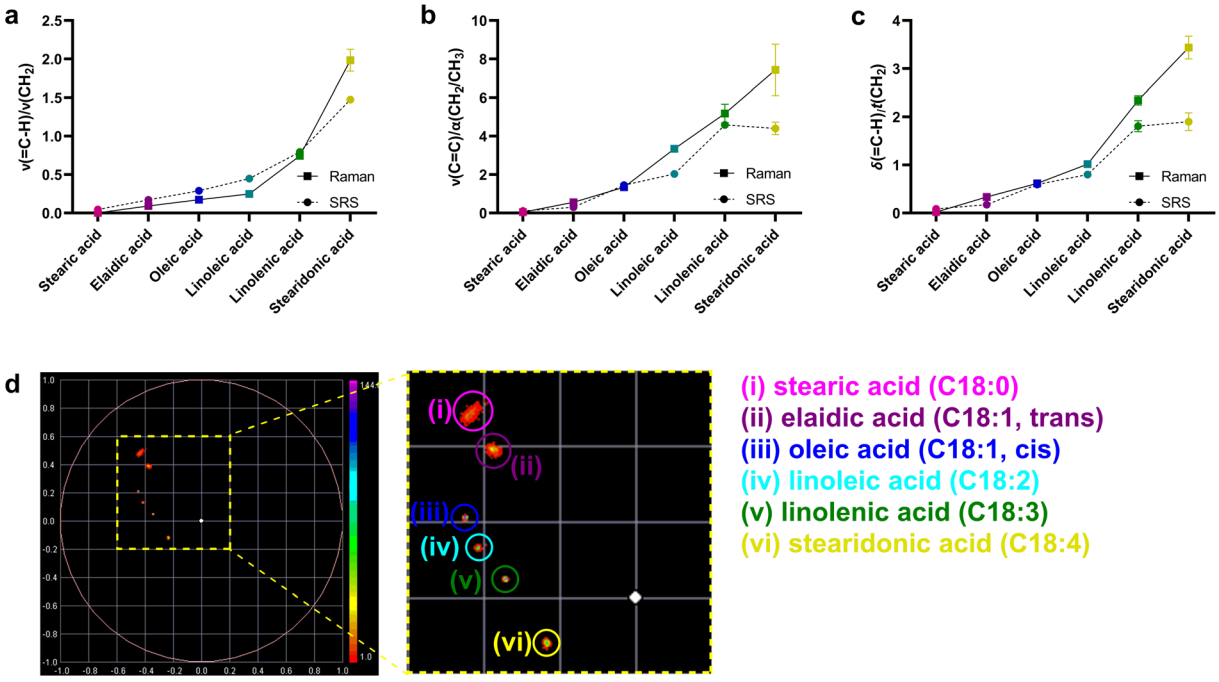

Fig. 2 Ratiometric Raman and spectral phasor analysis of fatty acids. Ratiometric analysis of the Raman intensities at (a) ν(=C–H)/$\nu(CH_2)$, (b) ν(C=C)/$\alpha(CH_2/CH_3)$ and (c) δ(=C–H)/$\tau(CH_2)$. Data represent the mean ratio from three independent repeats with error bars ± S.D. (d) Spectral phasor analysis of the six FAs using hyperspectral SRS imaging in the high wavenumber region (2800–3050 cm^{-1}). The yellow dashed marker highlights the region of the phasor plot that is expanded for clarity.

spectral phasor analysis. The spectral phasor plot showed clear separation between the different FAs (Fig. 2d). Stearic acid and elaidic acid were located furthest from the origin and showed the greatest spectral similarity, whilst across the series of *cis*-unsaturated FAs, the phasors clustered in a pattern towards the origin of the plot. This study is the first to demonstrate the segmentation of FAs based on hyperspectral SRS data using spectral phasor analysis and, when combined with ratiometric analysis of the SRS spectrum, it resulted in a powerful methodology for compositional lipid analysis.

Having validated the use of hyperspectral SRS imaging combined with spectral phasor analysis, we sought to investigate lipid composition in a cellular model of cancer and DIS. Firstly, HeLa cells were treated with DMSO (control) or FA (400 μM conjugated to 5% BSA in a 1 : 4 v/v ratio) prior to fixation with paraformaldehyde. Hyperspectral SRS imaging was performed across the high wavenumber region (2800–3050 cm^{-1}) and fingerprint region (1200–1780 cm^{-1}) of the Raman spectrum. From the image stacks, an average intensity projection was created, which provided a label-free overview of the cellular locations, together with a ratiometric image of the CH_2/CH_3 (2851/2930 cm^{-1}) content (Fig. 3a). The ratiometric analysis highlighted the nuclear region (weak CH_2/CH_3 signal, blue), the cytoplasm (intermediate CH_2/CH_3 ratio, green) and the cellular LDs (high CH_2/CH_3 ratio, red). We next performed spectral phasor analysis on the hyperspectral SRS images, to improve the segmentation of the LDs based on the known location of lipids in the phasor domain. Spectral phasor analysis revealed that the treatment with FAs resulted in the detection of larger lipid droplets compared to the control cells (Fig. 3b) and a larger % area of LDs per cell (Fig. 3c) compared to the control cells. In addition, treatment with the monounsaturated FAs, elaidic acid and oleic acid, resulted in more lipid droplets compared to the other FAs, reflecting the impact of unsaturation and lipid conformation upon intracellular uptake.

The use of spectral phasor analysis enabled a direct comparison of the LD composition in each case. In the high wavenumber region, the mean LD spectra showed an increasing intensity of the ν(=C–H) band at ~3010 cm^{-1} as the degree of

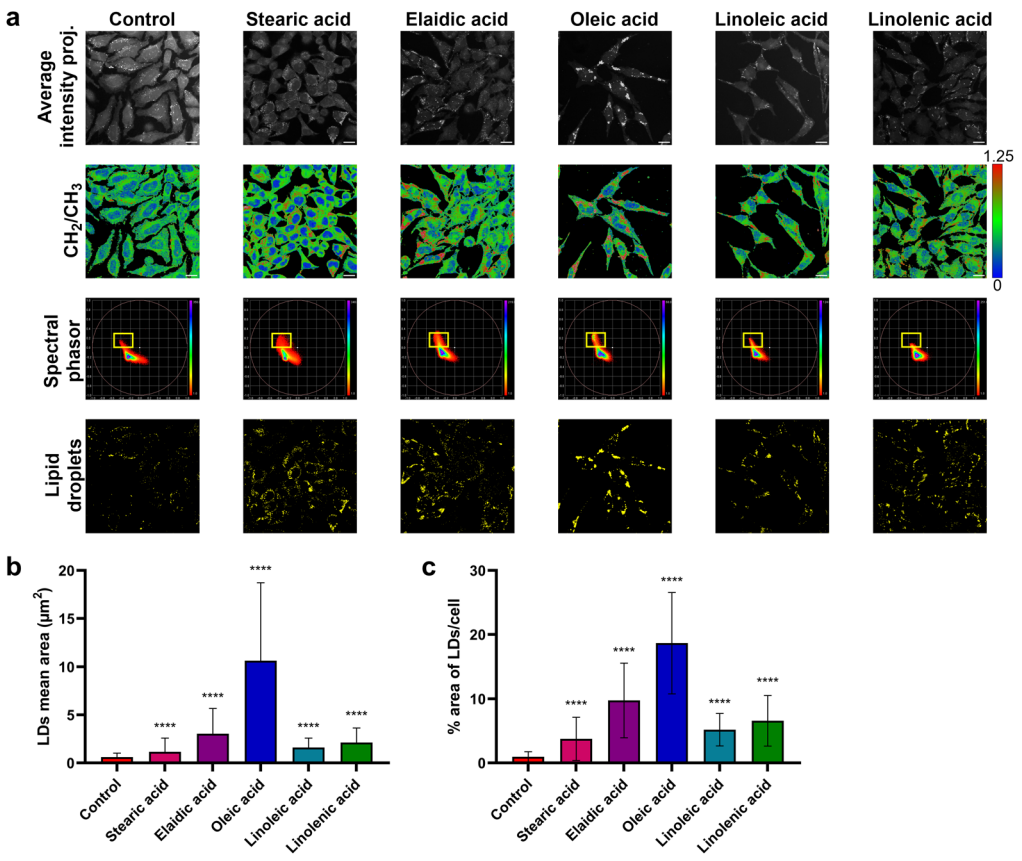

Fig. 3 Investigating lipid droplet composition using hyperspectral SRS imaging and spectral phasor analysis. HeLa cells were treated with DMSO (control cells) or the indicated fatty acid (400 μM, 24 h) prior to fixation with 4% paraformaldehyde. For each condition, three hyperspectral SRS image stacks were acquired in the high wavenumber region (2800–3050 cm^{-1}, 6.3 cm^{-1} increments) and fingerprint region (1200–1780 cm^{-1}, 7.5 cm^{-1} increments) of the SRS spectrum. (a) An average intensity projection from the high wavenumber region stack for each condition is presented alongside a ratiometric image of the CH_2/CH_3 and the segmented lipid droplets derived from the spectral phasor analysis (LDs: yellow marker). (b) Quantification of the mean area of LDs in HeLa cells under each condition. Data represent the mean area with error bars + S.D. from a minimum of three replicate areas (>30 cells). (c) Quantification of the % area of LDs per cell under each treatment condition. Data represent the mean % area with error bars ± S.D. from a minimum of three replicate areas (>30 cells).

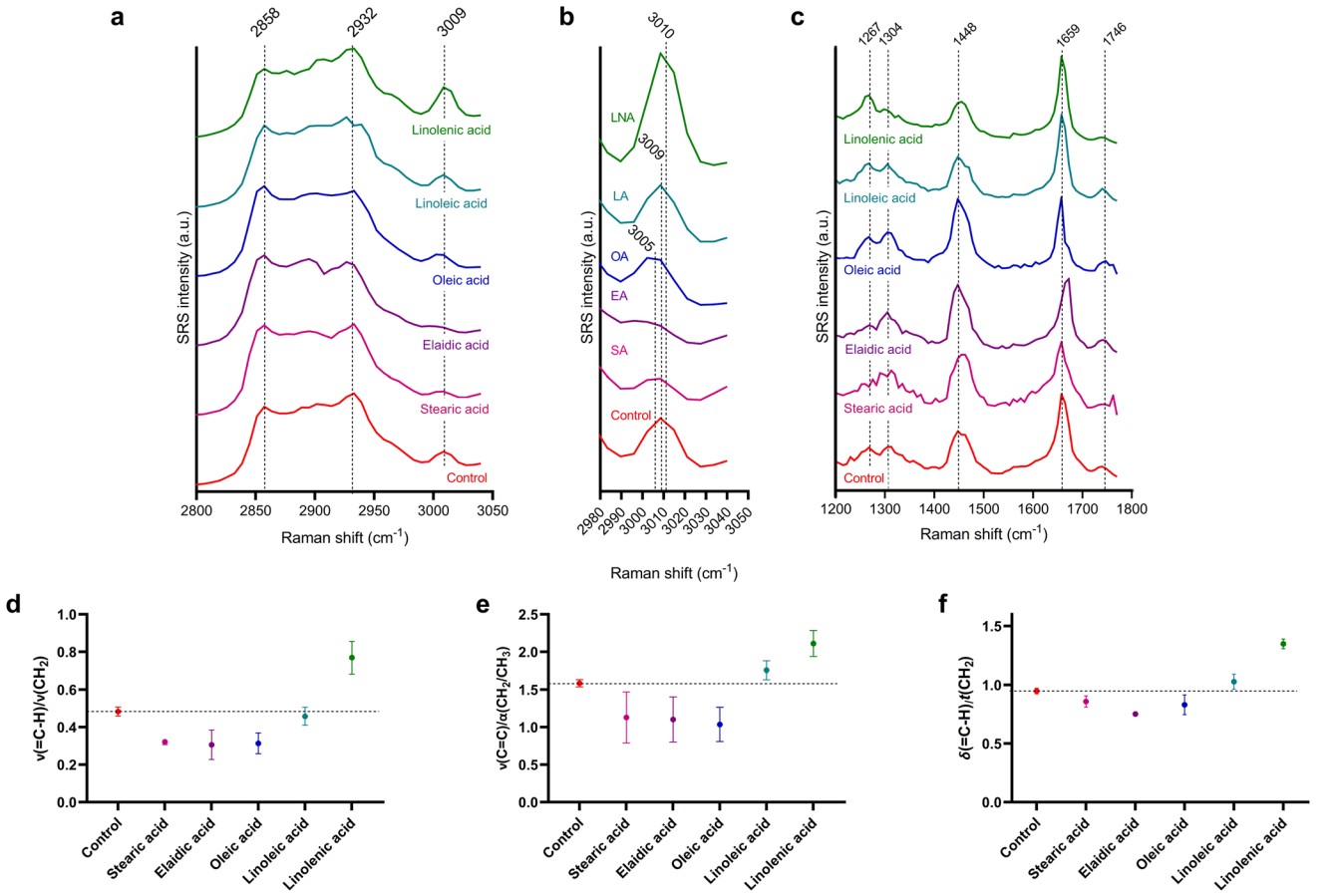

Fig. 4 Hyperspectral SRS imaging of HeLa cells treated with FAs. Spectral phasor analysis was used to segment the cellular LDs in the hyperspectral SRS image stacks from Fig. 3 and the corresponding average SRS spectra presented in the region (a) 2800–3050 cm^{-1}, (b) expansion of the region corresponding to ν(=C–H) at ~3010 cm^{-1} and (c) in the region 1200–1780 cm^{-1}. (d) Ratiometric analysis of the Raman bands ν(=C–H)/ν(CH_2) at ~3010 cm^{-1}/~2851 cm^{-1}, (e) ratiometric analysis of the Raman bands ν(C=C)/α(CH_2/CH_3) at ~1660 cm^{-1}/~1440 cm^{-1}, (f) ratiometric analysis of the Raman bands at δ(=C–H)/τ(CH_2) at ~1267 cm^{-1}/~1302 cm^{-1}. Data represent the mean ratio with error bars: ±S.D.

unsaturation of incubated FA increases (Fig. 4a and b). Interestingly, in the LD spectrum of cells treated with stearic acid and elaidic acid, the intensity of the ν(=C–H) band is lower than in the control cells. Together these results suggested that the FAs had become incorporated into the cellular LD pool. In the linolenic acid treated cells, the Raman band at ~2850 cm^{-1} (ν(CH_2)) was at a reduced intensity relative to the ν(CH_3) at ~2930 cm^{-1}, which is in agreement with the SRS spectra of the neat FA (Fig. 1a). In the fingerprint region, the intensity of the ν(C=C) increased relative to the α(CH_2/CH_3) with increasing unsaturation, further supporting the observation that the FAs have become incorporated into the cellular LDs. From the SRS spectra, it was again possible to perform ratiometric analysis as previously, which identified that the lipid droplets in the control HeLa cells contained a high degree of unsaturated lipids (dashed markers, Fig. 4d–f). In addition, we investigated the impact of varying the treatment concentration of oleic acid. HeLa cells were treated with oleic acid (0–400 μM, 24 h) and analysed by hyperspectral SRS microscopy (Fig. S1†). As indicated by the ratiometric analysis, at all oleic acid treatment concentrations tested, a lower ratio for the lipid unsaturation was observed when compared to the untreated control samples, which were acquired concomitantly and the results of which agreed with our observations in Fig. 4. Moreover, for each ratio tested, the results did not vary significantly between the treated cells, indicating that the LDs spectra and the resulting ratios are not dependent on the concentration or uptake in FAs, but only on the nature and unsaturation degree of the lipids. The SRS imaging presented here has a higher spatial resolution (~400 nm) compared to conventional Raman imaging systems (typically ~ 1 μm) which means that the detection of smaller LDs is more accurate and reproducible. When coupled to hyperspectral imaging with spectral phasor analysis, the improved spatial resolution minimises the potential contribution of the surrounding cytoplasm in cases where LDs are smaller than the laser spot size. Altogether, these data indicate that hyperspectral SRS imaging coupled to spectral phasor analysis is a powerful method for lipid characterisation in a cancer cell model.

Lastly, we investigated cellular steatosis in a hepatocarcinoma cell model. Hepatic steatosis, also called fatty liver disease (FLD), is characterised by an excess accumulation of

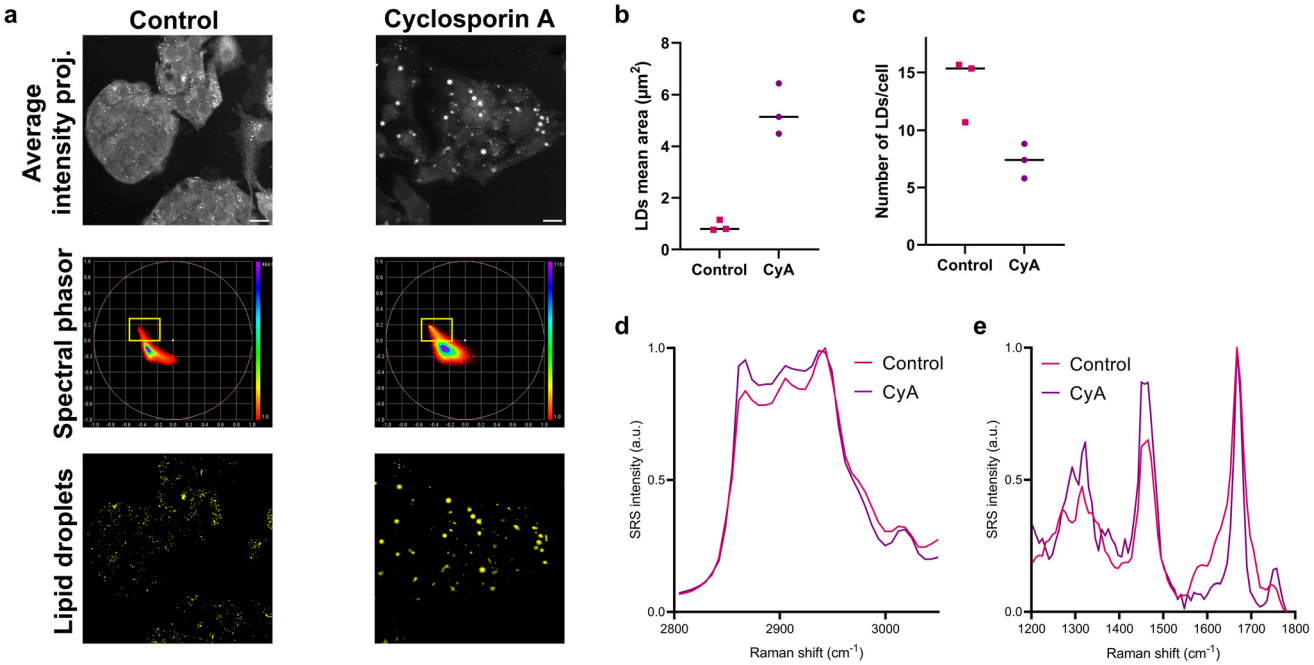

Fig. 5 Hyperspectral SRS imaging of drug-induced steatosis. HepG2 cells were treated with cyclosporin A (30 μM, 48 h) or DMSO (control) before fixing with paraformaldehyde (4% in PBS). Hyperspectral SRS images were acquired across the regions 2800–3050 cm^{-1} and 1200–1780 cm^{-1}. (a) An average intensity projection was created for the cells in each treatment condition, together with spectral phasor analysis of the cell population highlighting the lipid droplet region (yellow marker) from which the segmented LDs images were created. (b) Quantification of the mean area of all lipid droplets in three replicate fields of view using spectral phasor analysis. (c) Quantification of the mean number of LDs per cell from three replicate fields of view using spectral phasor analysis. (d and e) Normalised SRS spectra for the LDs in each condition retrieved by spectral phasor analysis. Spectra are normalised between 0–1.

fat in the liver and can be divided into two types: non-alcoholic FLD (NAFLD) or alcoholic liver disease. HepG2 cells were treated with cyclosporin A, an immunosuppressant drug known to induce lipid accumulation and steatosis in hepatocytes.[43] The cells were treated with 30 μM of cyclosporin A for 48 hours to mimic DIS, or with DMSO as a control. Thereafter, the fixed HepG2 cells were imaged by hyperspectral SRS imaging between 2800–3050 cm^{-1} and 1200–1780 cm^{-1} as in the previous experiments. Spectral phasor analysis was used to segment the lipid droplet pool in the cyclosporin A and control treated cells (Fig. 5a). The treatment of the cells with cyclosporin A did induce steatosis in the cells, which is illustrated by an increase in the LDs size (Fig. 5b), with the number of phasors related to the LDs (yellow marker) increasing in the treated cells. The results were confirmed by the calculation of the mean number of the LDs in the treated cells compared to the controls (Fig. 5c). The number of LDs per cell in the control HepG2 cells is higher than in the treated samples, indicating that steatosis induces the gathering of several LDs into larger structures. Together, these results confirmed that cyclosporin A treatment results in macrovesicular steatosis,[44] through the presence of fewer, but larger, LDs per cell compared to the control cells. In addition, the SRS spectra indicated that the degree of unsaturation decreased in the larger lipid droplets associated with cyclosporin A treatment: the intensity of the $\alpha(CH_2/CH_3)$ and $\tau(CH_2)$ modes are much greater in the cyclosporin A spectra compared to the control cells. In addition, the detection of an intense $\nu(C{=}O)$ at ~1740 cm^{-1} indicated the esterification of fatty acids, likely into triacylglycerols (TAGs) or the presence of cholesterol esters.[41] Our results have demonstrated the potential of hyperspectral SRS imaging combined with spectral phasor analysis for studying lipid composition in the high wavenumber and fingerprint region with molecular specificity. Our method has demonstrated the benefit of spectral phasor analysis, to enable the discrimination of 6 FAs in neat form, and to enable the intracellular visualisation of FAs into cellular samples. As such, this system has enabled access to imaging across a greater rage of the SRS spectrum for lipid profiling compared to two previous reports using the fingerprint region (1070–1120 cm^{-1})[15] and the high wavenumber region (2800–3050 cm^{-1}).[34]

Conclusions

We have demonstrated the application of hyperspectral SRS imaging in the high wavenumber and fingerprint regions of the Raman spectrum for the characterisation of FA uptake and distribution in HeLa cells, and to visualise cellular steatosis. The application of spectral phasor analysis enabled robust segmentation of the lipid droplets in each case to enable direct

comparison of the corresponding SRS spectra across a broader range of the spectrum than has been demonstrated previously. By capitalising on the high spatial resolution associated with SRS microscopy, label-free detection of FA uptake was achieved across a larger sample coverage than would be realistically achieved using spontaneous Raman imaging. We propose that the automation of spectral phasor analysis could be integrated into SRS imaging applications for multidimensional cellular profiling in real-time.

Data availability

The research data associated with this paper will become available from the University of Strathclyde at the following link: **https://doi.org/10.15129/316368b3-e325-4c93-911c-f19a83dca79d**.

Author contributions

A. R. and W. J. T. performed all experiments, analysed the results, and wrote the manuscript. W. J. T. devised the project. C. M., K. F., G. E. and D. G. supervised the project. K. F. and D. G. are responsible for funding.

Conflicts of interest

There are no conflicts to declare.

Acknowledgements

We thank the University of Strathclyde and the EPSRC (EP/TR512114/1) for financial support.

Notes and references

1 J. A. Olzmann and P. Carvalho, *Nat. Rev. Mol. Cell Biol.*, 2019, **20**, 137–155.
2 T. C. Walther, J. Chung and R. V. Farese, Jr., *Annu. Rev. Cell Dev. Biol.*, 2017, **33**, 491–510.
3 O. Quehenberger and E. A. Dennis, *N. Engl. J. Med.*, 2011, **365**, 1812–1823.
4 T. Sassa and A. Kihara, *Biomol. Ther.*, 2014, **22**, 83–92.
5 N. L. Gluchowski, M. Becuwe, T. C. Walther and R. V. Farese, Jr., *Nat. Rev. Gastroenterol. Hepatol.*, 2017, **14**, 343–355.
6 S. Cockcroft, *Essays Biochem.*, 2021, **65**, 813–845.
7 N. Koundouros and G. Poulogiannis, *Br. J. Cancer*, 2020, **122**, 4–22.
8 F. Rohrig and A. Schulze, *Nat. Rev. Cancer*, 2016, **16**, 732–749.
9 A. R. Buchberger, K. DeLaney, J. Johnson and L. Li, *Anal. Chem.*, 2018, **90**, 240–265.
10 J. Li, T. Vosegaard and Z. Guo, *Prog. Lipid Res.*, 2017, **68**, 37–56.
11 D. Tsikritsis, E. J. Legge and N. A. Belsey, *Analyst*, 2022, **147**, 4642–4656.
12 W. J. Tipping, M. Lee, A. Serrels, V. G. Brunton and A. N. Hulme, *Chem. Soc. Rev.*, 2016, **45**, 2075–2089.
13 J.-X. Cheng and X. S. Xie, *Science*, 2015, **350**, aaa8870.
14 Y. Shen, L. Wei and W. Min, *J. Phys. Chem. B*, 2023, **127**, 6233–6240.
15 Z. Huang, S. Yan, Y. Li, W. Ju and P. Wang, *Anal. Chem.*, 2023, **95**, 5815–5819.
16 J. Yoon, S.-w. Ryu, S. Lee and C. Choi, *Sci. Rep.*, 2015, **5**, 8231.
17 J. Du, Y. Su, C. Qian, D. Yuan, K. Miao, D. Lee, A. H. C. Ng, R. S. Wijker, A. Ribas, R. D. Levine, J. R. Heath and L. Wei, *Nat. Commun.*, 2020, **11**, 4830.
18 C. Zhang, J. Li, L. Lan and J.-X. Cheng, *Anal. Chem.*, 2017, **89**, 4502–4507.
19 D. Fu, Y. Yu, A. Folick, E. Currie, R. V. Farese, T.-H. Tsai, X. S. Xie and M. C. Wang, *J. Am. Chem. Soc.*, 2014, **136**, 8820–8828.
20 S. Yan, S. Cui, K. Ke, B. Zhao, X. Liu, S. Yue and P. Wang, *Anal. Chem.*, 2018, **90**, 6362–6366.
21 Y. Li, W. Zhang, A. A. Fung and L. Shi, *Analyst*, 2021, **146**, 7510–7519.
22 S. Egoshi, K. Dodo and M. Sodeoka, *Curr. Opin. Chem. Biol.*, 2022, **70**, 102181.
23 A. N. von Krusenstiern, R. N. Robson, N. Qian, B. Qiu, F. Hu, E. Reznik, N. Smith, F. Zandkarimi, V. M. Estes, M. Dupont, T. Hirschhorn, M. S. Shchepinov, W. Min, K. A. Woerpel and B. R. Stockwell, *Nat. Chem. Biol.*, 2023, **19**, 719–730.
24 M. Uematsu, Y. Kita, T. Shimizu and H. Shindou, *FASEB J.*, 2020, **34**, 10357–10372.
25 C. Matthäus, C. Krafft, B. Dietzek, B. R. Brehm, S. Lorkowski and J. Popp, *Anal. Chem.*, 2012, **84**, 8549–8556.
26 L. E. Jamieson, J. Greaves, J. A. McLellan, K. R. Munro, N. C. O. Tomkinson, L. H. Chamberlain, K. Faulds and D. Graham, *Spectrochim. Acta, Part A*, 2018, **197**, 30–36.
27 S. Hong, T. Chen, Y. Zhu, A. Li, Y. Huang and X. Chen, *Angew. Chem., Int. Ed.*, 2014, **53**, 5827–5831.
28 L. Wei, F. Hu, Y. Shen, Z. Chen, Y. Yu, C.-C. Lin, M. C. Wang and W. Min, *Nat. Methods*, 2014, **11**, 410–412.
29 A. Alfonso-García, J. Paugh, M. Farid, S. Garg, J. Jester and E. Potma, *J. Raman Spectrosc.*, 2017, **48**, 803–812.
30 P. Wang, B. Liu, D. Zhang, M. Y. Belew, H. A. Tissenbaum and J.-X. Cheng, *Angew. Chem.*, 2014, **126**, 11787–11792.
31 E. W. Hislop, W. J. Tipping, K. Faulds and D. Graham, *Anal. Chem.*, 2022, **94**, 8899–8908.
32 D. Fu and X. S. Xie, *Anal. Chem.*, 2014, **86**, 4115–4119.
33 M. Wei, L. Shi, Y. Shen, Z. Zhao, A. Guzman, L. J. Kaufman, L. Wei and W. Min, *Proc. Natl. Acad. Sci. U. S. A.*, 2019, **116**, 6608–6617.
34 W. J. Tipping, L. T. Wilson, C. An, A. A. Leventi, A. W. Wark, C. Wetherill, N. C. O. Tomkinson, K. Faulds and D. Graham, *Chem. Sci.*, 2022, **13**, 3468–3476.

35 H. J. Braddick, W. J. Tipping, L. T. Wilson, H. S. Jaconelli, E. K. Grant, K. Faulds, D. Graham and N. C. O. Tomkinson, *Anal. Chem.*, 2023, **95**, 5369–5376.
36 E. W. Hislop, W. J. Tipping, K. Faulds and D. Graham, *Anal. Chem.*, 2023, **95**, 7244–7253.
37 B. Wong, X. Zhao, Y. Su, H. Ouyang, T. Rhodes, W. Xu, H. Xi and D. Fu, *Mol. Pharm.*, 2023, **20**, 4268–4276.
38 N. Murphy, W. J. Tipping, H. J. Braddick, L. T. Wilson, N. C. O. Tomkinson, K. Faulds, D. Graham and P. Farràs, *Angew. Chem., Int. Ed.*, 2023, e202311530.
39 A. L. S. Cruz, E. d. A. Barreto, N. P. B. Fazolini, J. P. B. Viola and P. T. Bozza, *Cell Death Dis.*, 2020, **11**, 105.
40 S. K. Satapathy, V. Kuwajima, J. Nadelson, O. Atiq and A. J. Sanyal, *Ann. Hepatol.*, 2015, **14**, 789–806.
41 K. Czamara, K. Majzner, M. Z. Pacia, K. Kochan, A. Kaczor and M. Baranska, *J. Raman Spectrosc.*, 2015, **46**, 4–20.
42 L. T. Wilson, W. J. Tipping, C. Wetherill, Z. Henley, K. Faulds, D. Graham, S. P. Mackay and N. C. O. Tomkinson, *Anal. Chem.*, 2021, **93**, 12786–12792.
43 M. M. Angrish, C. A. McQueen, E. Cohen-Hubal, M. Bruno, Y. Ge and B. N. Chorley, *Toxicol. Sci.*, 2017, **159**, 159–169.
44 T. Minamikawa, M. Ichimura-Shimizu, H. Takanari, Y. Morimoto, R. Shiomi, H. Tanioka, E. Hase, T. Yasui and K. Tsuneyama, *Sci. Rep.*, 2020, **10**, 18548.